Available online at www.sciencedirect.com
ScienceDirect
International Journal of Heat and Fluid Flow 29 (2008) 178–193
International Journal of HEAT AND FLUID FLOW
www.elsevier.com/locate/ijhff

Interfacial area transport of vertical upward air–water two-phase flow in an annulus channel

J.J. Jeong [a,*], B. Ozar [b], A. Dixit [b], J.E. Juliá [c], T. Hibiki [b], M. Ishii [b]

[a] Korea Atomic Energy Research Institute, 150 Deokjin, Yuseong, Daejeon 305-353, Republic of Korea
[b] School of Nuclear Engineering, Purdue University, 400 Central Drive, West Lafayette, IN 47907, USA
[c] Dept. de Ingeniería Mecánica y Construcción, Universitat Jaume I. Castellón, Spain

Received 18 January 2007; received in revised form 10 July 2007; accepted 13 July 2007
Available online 18 September 2007

Abstract

An experimental study on the interfacial area transport (IAT) of vertical, upward, air–water two-phase flows in an annulus channel has been conducted. The inner and outer diameters of the annular channel were 19.1 mm and 38.1 mm, respectively. Nineteen inlet flow conditions were selected, which cover bubbly, cap–slug, and churn–turbulent flows. The local flow parameters, such as void fraction, interfacial area concentration (IAC), and bubble interface velocity, were measured at nine radial positions for the three axial locations ($z/D_H = 52$, 149 and 230). The radial and axial evolutions of local flow structure were interpreted in terms of bubble coalescence and breakup. The measured data can be used for the development of the bubble coalescence/breakup models for the IAT model and some closure models for computational fluid dynamics.

Keywords: Interfacial area concentration; Local flow measurement; Annulus; Bubbly flow; Cap–slug flow; Churn–turbulent flow

1. Introduction

In the two-fluid model for two-phase flow, liquid and gas phases are separately described by using two sets of conservation equations for mass, momentum and energy. The equations are linked by interfacial transfer terms, which represent the mass, momentum, and energy transfer at the liquid–vapor interface. These terms are generally given by the product of the IAC and the local transfer rate per interfacial area. The IAC is defined by interfacial area per unit volume of two-phase mixture. In most of the nuclear system analysis codes like RELAP5 (SCIENTECH, Inc., 1998), TRAC-PF1 (Spore et al., 1993), and CATHARE (Bestion, 1990), or computational multi-fluid dynamic codes like CFX that adopt the two-fluid model for two-phase flows, the IAC has been modeled by using flow regime transition criteria and regime-dependent constitutive relations. For example, both RELAP5 and TRAC use the flow regime maps, which represent the interfacial structure including the IAC in terms of a geometric parameter of the flow, the phasic velocities, and the void fraction only. The maps were developed from fully developed, steady-state conditions and, however, these are applied to both developing and transient flows. These maps do not take into account time or length scale for the flow regime transition and, instead, arbitrary smoothing functions at the boundary between two flow regimes are used to avoid numerical instabilities. These features have driven the interfacial structure of the system codes less physical, deteriorating the real advantages of two-fluid model. The limitations of the flow regime map approach have been discussed in detail by Uhle et al. (1998) and Hibiki and Ishii (2000). This was also pointed out by Ishii (1975) very early and he suggested a transport equation for interfacial area.

Recent advances in two-phase measurement have stimulated further research on IAT model. Especially, the

* Corresponding author. Tel.: +82 42 868 2958; fax: +82 42 868 8990.
E-mail address: jjjeong@kaeri.re.kr (J.J. Jeong).

0142-727X/$ - see front matter © 2007 Elsevier Inc. All rights reserved.
doi:10.1016/j.ijheatfluidflow.2007.07.007

improvement of double- and four-sensor conductivity probes (Kataoka et al., 1986; Revankar and Ishii, 1993; Wu and Ishii, 1999; Kim et al., 2000) allowed accurate measurement of local two-phase flow parameters, such as void fraction, interfacial area concentration, interfacial velocity, etc. This, in turn, has resulted in the improvement of IAT models (Kocamustafaogullari and Ishii, 1995; Morel et al., 1999; Hibiki and Ishii, 2000; Fu, 2001; Sun et al., 2004a).

The formulation of IAT equations is based on statistical mechanics and its concept has been fully established (Ishii et al., 2005; Ishii and Hibiki, 2006). However, the source and sink terms of interfacial area due to bubble coalescence and breakup are still being developed. These are strongly dependent on flow conditions and geometries. So far, most of the experiments for interfacial area research have been performed in round tubes (Revankar and Ishii, 1992; Grosstete, 1995; Hibiki et al., 1998, 2001; Hibiki and Ishii, 1999, 2000; Fu, 2001; Smith, 2002; Ishii and Kim, 2004; Ishii et al., 2005; Yao and Morel, 2004). Fig. 1 summarizes the experimental conditions of the above-mentioned interfacial area studies in round tubes.

Two-phase flows in annular channels are frequently encountered in industrial applications. In addition, the study of the flow in the annular channel provides a basis for investigations of the flow through more complicated geometries like the shell side of a shell and tube heat exchanger and the rod bundle of a nuclear reactor. This has motivated extensive research on the two-phase flow in annular channels for flow-regime (Kelessidis and Dukler, 1989; Das et al., 1999; Sun et al., 2004b), pressure drop, interfacial drag, critical heat flux, etc. However, there are very few experimental data for interfacial area research in an annulus channel. Hibiki et al. (2003) performed experiments, but their flow conditions were limited to bubbly flows.

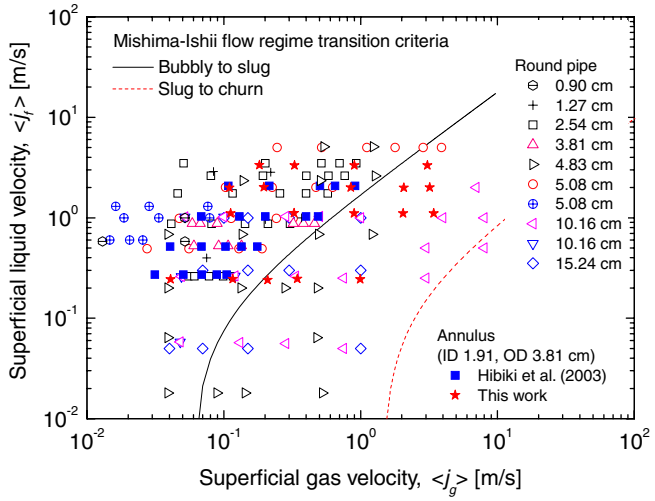

Fig. 1. Experimental conditions for interfacial area research in round pipes and annuli: inlet flow conditions are given.

In this work, an experimental study on the IAT of vertical, upward, air–water two-phase flows in an annular channel under bubbly, cap–slug, and churn–turbulent flows has been conducted. The annular test section consists of an inner rod of 19.1 mm diameter and an outer tube with an inside diameter of 38.1 mm. The test section is 4.37 m long, which is 2.3 m longer than that of Hibiki et al. (2003), whereas the cross section is the same. Nineteen inlet flow conditions, marked with stars in Fig. 1, were selected so that a wide range of flow conditions can be covered. Four-sensor conductivity probes, instead of the double-sensor conductivity probes that were used in the experiments of Hibiki et al. (2003), were adopted to measure local flow parameters at nine radial positions of three axial locations. These include local void fractions, interfacial area concentrations, and interfacial velocities for two groups of bubbles; spherical and distorted bubbles as Group 1, whereas cap, slug and churn–turbulent bubbles as Group 2. Using the experimental data that are unique and of practical importance, the radial profile of two-phase interfacial structure and its axial evolution have been investigated.

2. Experimental facility and instrumentations

The experimental facility was designed to measure the local and global two-phase flow parameters under either adiabatic air–water two-phase flow or subcooled boiling conditions. The annular test section of the facility is a scaled prototypic boiling water nuclear reactor (BWR) based on geometric and thermal-hydraulic similarities (Situ et al., 2004). Fig. 2 shows the schematic of the experimental facility. Since this study focused on adiabatic air–water tests, the components that are concerned with heating, cooling, and pressurization were not shown. The air–water separator is open to the atmosphere.

The test section is composed of an injection port, an annular flow channel of 4.37 m length, and five measurement ports. Using the test section, two-phase flow behaviors in a full-length BWR fuel channel can be investigated. The annular channel consists of an inner rod with a diameter of 19.1 mm and a transparent tube with an inner diameter of 38.1 mm. The equivalent hydraulic diameter, D_H, is 19.0 mm. Each measurement port has a four-sensor conductivity probe, an impedance meter, and a thermocouple. The port was designed so that the conductivity probe can be radially traversed in the annulus gap. Port 1, 3, and 5 ($z/D_H = 52$, 149 and 230, respectively) were used for local flow measurements, where z is the axial distance from the inlet of the test section. The pressure at the injection port and the differential pressure between each measurement port and the inlet are also measured.

The bypass section, directly connecting the exit of the pump to the bottom exit of the condenser, was designed such that it carries 5–10 times of the flow rate through the test section. The reason for this is to maintain constant pressure boundary conditions across the test section, resulting in a constant flow rate through the test section.

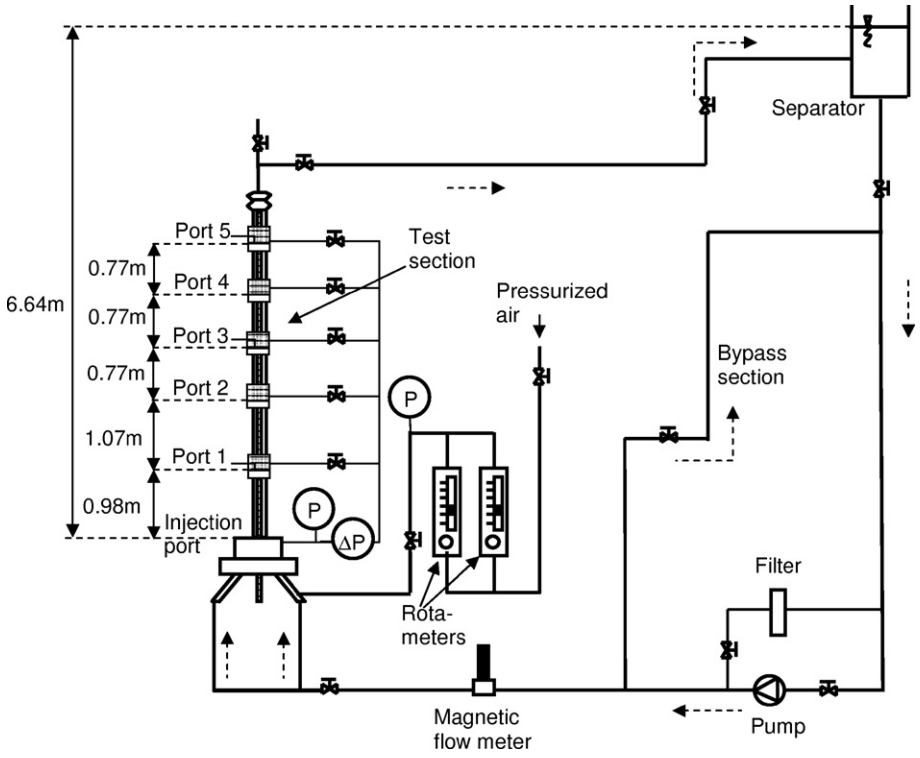

Fig. 2. The schematic of the test facility.

Filtered and chemically treated water was used during the experiments. The city water was first passed through resin filters for purification and de-ionization. However, the electrical conductivity dropped almost to zero after this process. Since the conductivity probe measurements were electrical based and required some conductivity, additional chemical treatment was needed. Ammonium hydroxide and morpholine were added into the water. Finally, a conductivity of 60 μS and pH 8.5 were achieved. Surface tension of the treated water was checked by using the pendant drop method described by Matijevic (1969). The measured surface tension was 0.073 N/m. In comparison to that of the distilled water, the difference of 3% was found to be less than the uncertainty of the measurement technique.

The water flow rate to the test section is controlled by adjusting the pump speed, the globe valve on the inlet line to the test section and the bypass valve. The flow rate is measured by using a magnetic flow meter with an uncertainty of ±1%. Before the water enters into the test section, it is introduced through a header, which divides the flow in four separate lines. Air is supplied from an external system. The air flow rate is controlled by four rotameters with different maximum ranges of volumetric flow. They can measure the flow rate with an accuracy of ±3% when the flow rate is greater than 50% of the full scale. A pressure gage is installed at the exit of the rotameters to measure the back pressure. The air line, leaving the pressure gauge, is divided into four separate lines. An air line and a water line are connected to an air–water mixing unit of the injection port, which is shown in Fig. 3. The mixing unit is composed of a tee, a sparger with mean pore size of 10-μm, and a nipple. In this unit, air bubbles are sheared off from the spargers by the water in the nipple. The bubble sizes at the mixing unit cannot be regulated, but expected to be about 2–3 mm. This can be regarded as an independent parameter for flow conditions. The Sauter mean diameter of Group1 bubbles at $z/D_H = 52$ ranges from 1.6 to 3.7 mm, which was dependent on the water velocity.

The local flow parameters, such as, void fraction, bubble interface velocity and IAC, were measured with four-sensor conductivity probes at $z/D_H = 52$, 149 and 230. Fig. 4 shows the schematic of the conductivity probe. The probe cross-sectional area is so small in comparison with the flow area that it may not affect the downstream flow so much. At each axial location, the probe was traversed in the radial direction to measure at nine radial positions; $(r - R_i)/(R_0 - R_i) = 0.1, 0.2, \ldots, 0.9$, where r, R_i, and R_0 are the radial distance from the centerline of the annulus, the radius of the inner rod, and the inside radius of the outer tube, respectively. The last radial position at $z/D_H = 149$ was adjusted slightly more inside because of the probe size.

The conductivity probe, proposed by Neal and Bankoff (1963), is based on the difference of conductivity between water and air. The local time-averaged void fraction can be obtained by dividing the sum of the time fraction occupied by gas-phase by the total measurement time. The bubble interface velocity can be obtained by using the two sensors (sensors 0 and 1 in Fig. 4) of the conductivity probe. This measurement is performed by utilizing the ratio

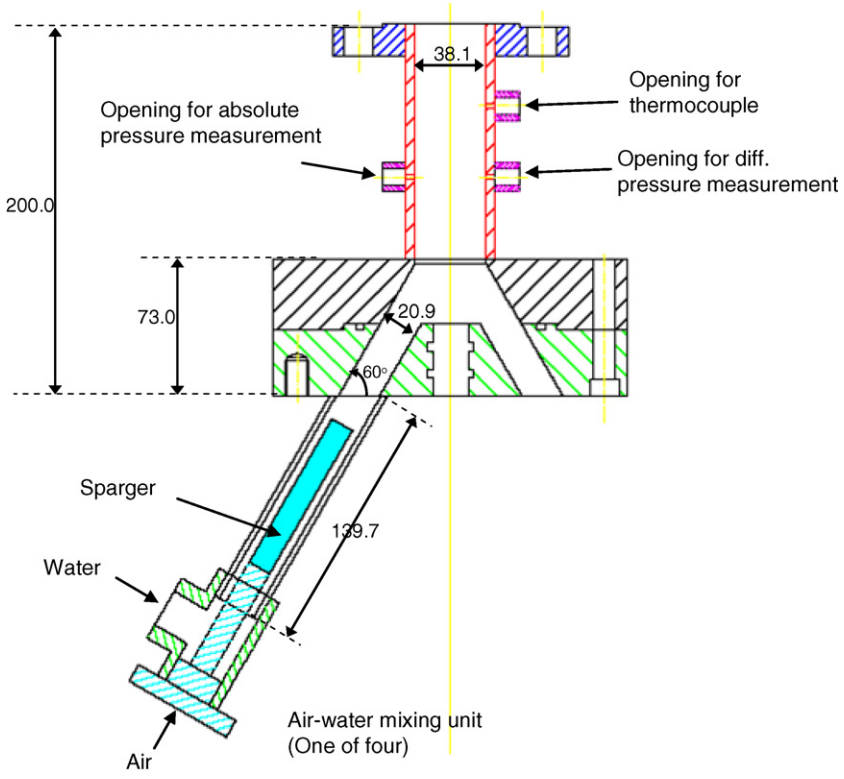

Fig. 3. The injection port (dimensions in mm).

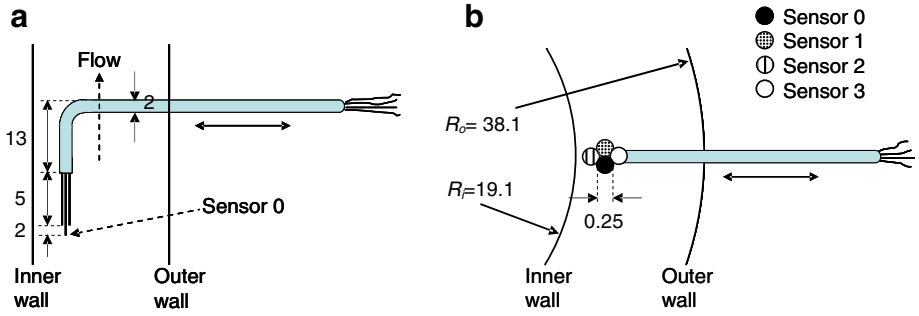

Fig. 4. A schematic of the conductivity probe (dimensions in mm, not scaled). (a) Side view and (b) Bottom view.

of the distance between sensors 0 and 1 and the time delay that the bubble reaches to these sensor. This value is related to the local time-averaged interfacial area concentration with some assumptions and statistical considerations. The mathematical bases are provided by Ishii (1975) and Kataoka et al. (1986). It is noted that the double-sensor conductivity probe method (Wu and Ishii, 1999; Kim et al., 2001) adopts two assumptions; (i) the bubbles are spherical in shape, and (ii) every part of the bubble has equal probability of being intersected by the probe. As a result of the first assumption, the application of double-sensor probe is limited for only spherical bubbles.

In order to overcome this limitation, the four-sensor conductivity probe was proposed (Kataoka et al., 1986; Revankar and Ishii, 1993; Kim et al., 2000). In a four-sensor conductivity probe, three pairs of double sensors can be formed with one front common sensor in the upstream and three rear sensors in the downstream. Therefore, three components of interfacial velocities can be obtained at a local point by measuring the time delay between the signals from three pairs of double sensors. These are used to obtain the IAC without any assumptions (Ishii and Kim, 2001). However, the four-sensor probe has some practical limitations. These were caused by the probe configuration, resulting in a significant number of bubbles failing to penetrate all of the sensors. It was also reported that due to the bulky structure of the sensor arrangement and the sensor tips, the deformation of the bubble interface could be significant as the bubble penetrates through the sensors. Thus, the application of the four-sensor probe had been limited to larger bubbles. These deficiencies were resolved by developing sharp and highly conductive sensor tips and the min-

iaturized structure of the probe configuration (Kim et al., 2001). The significant reduction in the cross-sectional measurement area of the newly designed probe and its sharply tapered tips of the sensors could effectively minimize both the number of missing bubbles and the deformation of passing bubble interfaces. The probe size in this experiment was further reduced as illustrated in Fig. 4.

For the conductivity probe signal processing of the present study (Kim et al., 2001; Fu, 2001), bubbles are divided into two groups; spherical and distorted bubbles as Group 1, whereas cap, slug, and churn–turbulent bubbles as Group 2. The boundary between the two groups is determined by the maximum distorted bubble diameter specified by Ishii and Zuber (1979):

$$D_{\mathrm{d,max}} = 4\left(\frac{\sigma}{g\Delta\rho}\right)^{0.5}, \tag{1a}$$

where σ, g, and $\Delta\rho$ are the surface tension, gravitational acceleration, and the density difference between two phases. This grouping is based on shape and drag characteristics. If a bubble diameter becomes greater than the above diameter (e.g., 10.9 mm at 25 °C air–water flow under atmospheric pressure), the bubble becomes cap in shape and the drag effect starts to deviate from that on the smaller bubbles due to the large wake region. It is noted that Eq. (1a) was based on results obtained for pipe flows. The validity of the equation for two-phase flows in an annular channel needs to be justified. Furthermore the annulus gap size is slightly smaller than the maximum distorted bubble diameter in this experiment. But a bubble can expand up to the maximum distorted bubble diameter in axial and azimuthal directions without being confined by walls and, thus, it was assumed that Eq. (1a) can be used in the analysis of this experiment. Also, the data was reanalyzed by using the maximum distorted bubble diameter in a small gap specified by Sun et al. (2004a),

$$D_{\mathrm{d,max}} = 1.7G^{1/3}\left(\frac{\sigma}{g\Delta\rho}\right)^{1/3}, \tag{1b}$$

where G is the gap size in meter. But, this modification did not change the results significantly, because there were not so many bubbles around the Group 1 and Group 2 boundary. In order to obtain the IAC, the double-sensor (sensor 0 and 1) signals are used for Group 1 bubbles, and the four-sensor signals for Group 2 bubbles. This combination was devised to take advantage of the two methods. In order to test the reliability of this method, the conductivity probe was benchmarked earlier by a number of images, and the resulting relative differences for area averaged void fraction and IAC were within ±10% (Hibiki et al., 1998; Kim et al., 2001; Fu, 2001).

3. Experimental results and discussions

3.1. Experimental conditions

A study of air–water two-phase flow regimes has been independently performed using the same test facility by Juliá et al. (2007). Based on the results, nineteen inlet flow conditions were selected, which cover bubbly, cap–slug, and churn–turbulent flow regimes. The experimental conditions are summarized in Table 1. For the conductivity probe measurement, the data acquisition time was adjusted in each flow condition so that at least 2000 spherical bubbles and 200 slug bubbles were encountered by the front sensor. After a steady state was achieved for each test,

Table 1
The test conditions

Run no.	Superficial velocities (m/s)				Absolute pressure (kPa)			Data acquisition time (s)
	Water	Air						
		$z/D_{\mathrm{H}} = 52$	$z/D_{\mathrm{H}} = 149$	$z/D_{\mathrm{H}} = 230$	$z/D_{\mathrm{H}} = 52$	$z/D_{\mathrm{H}} = 149$	$z/D_{H} = 230$	
1	0.258	0.041	0.046	0.052	149.4	132.9	118.9	180
2	0.246	0.118	0.131	0.144	143.4	128.9	117.3	120
3	0.240	0.209	0.230	0.252	141.6	128.6	117.7	60
4	0.247	0.345	0.378	0.409	137.2	125.2	115.8	45
5	0.247	1.003	1.072	1.131	125.7	117.6	111.4	60
6	1.107	0.112	0.128	0.145	156.5	137.3	121.3	60
7	1.111	0.326	0.370	0.416	152.5	134.5	119.6	45
8	1.107	0.896	1.011	1.134	148.7	131.7	117.4	90
9	1.107	2.059	2.318	2.590	143.8	127.8	114.3	120
10	1.107	3.432	3.897	4.424	146.8	129.3	113.9	120
11	1.992	0.110	0.128	0.149	166.5	143.1	122.9	60
12	2.007	0.196	0.229	0.266	166.0	142.6	122.5	40
13	1.996	0.850	0.993	1.164	163.8	140.2	119.6	40
14	1.992	2.075	2.460	2.957	169.2	142.7	118.7	90
15	2.000	3.212	3.857	4.764	177.2	147.5	119.4	90
16	3.336	0.182	0.219	0.268	191.0	158.5	129.6	30
17	3.321	0.329	0.400	0.494	187.6	154.3	124.7	30
18	3.321	0.901	1.101	1.386	190.9	156.2	124.0	30
19	3.306	3.056	3.890	5.433	235.5	185.0	132.4	30

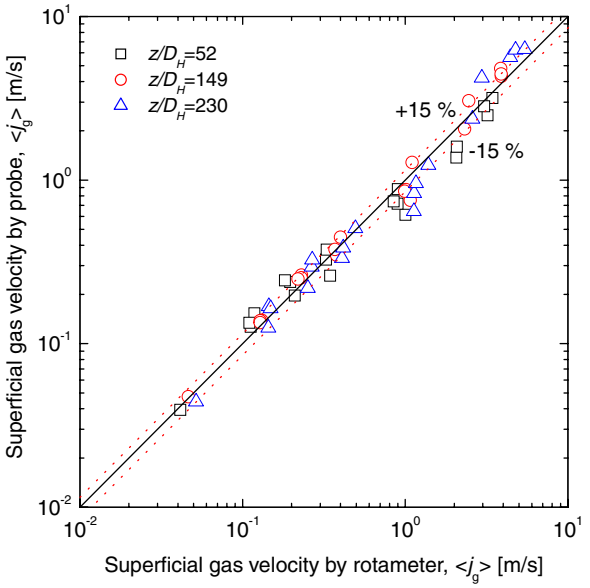

Fig. 5. Comparison of the local superficial gas velocities: the probe vs. the rotameter.

the probe at each axial location was radially traversed to measure at nine radial positions. The water temperature was maintained at about 25 °C.

As one of the methods to assess the local data measurement, the area-averaged local superficial gas velocities, $\langle j_g \rangle$, were calculated using the conductivity probe data obtained from the nine radial positions. Due to the finite size of the probe, it was not allowed to access the wall very closely. Thus, the local flow parameters near the wall were approximated by linear or second-order curves. But, the maximum difference between the two approximations was less than ±1%. The resulting superficial gas velocities were compared with those from the measurement of the rotameters and the local differential pressure gauges. Fig. 5 shows that they are relatively in good agreement with the average difference of 16.3%. This difference is slightly greater than that of Hibiki et al. (2003), where a similar test section was used. However, their test flow conditions remained at bubbly flows only. Fig. 5 also shows the differences at three axial positions are very similar to each other.

It is noted that the inlet flow conditions of Run 1, 2, 6, 7, and 11 were selected similar to those of Hibiki et al. (2003) for comparison. Although the design of air–water mixing unit and the axial and radial measurement positions were different in the two experiments, the radial void profile, area-averaged void fraction, the IAC under bubbly flow conditions at $z/D_H = 99$ (Hibiki et al., 2003) were very close to those of this experiments at $z/D_H = 149$.

3.2. Global flow regime

Two-phase flow in the present annular test section has two distinct features. First, the pressure drop by gravity and friction is not negligible because of the 4.37 m length of the test section. This entails the expansion of air, resulting in a continuous flow development along the test section. Second, the annulus gap size of 9.5 mm is smaller than the maximum distorted bubble diameter of about 10 mm, which is given in Eq. (1a). Thus, a growing bubble is to be radially confined by the inner and outer walls before it reaches the maximum distorted bubble. If the bubble grows further it becomes a cap bubble squeezed by the inner and outer walls. The shape of slug bubble is also different from that in a round pipe. It has been observed that big bubbles with a diameter close to the channel size can wrap the inner tube, but they can not cover the inner tube completely. Thus, the cap and slug bubbles are not distinguishable in this test section.

Based on the second feature, the flow regimes in the annular channel are divided into four categories (Juliá et al., 2007); bubbly (B), cap–slug (S), churn–turbulent (C), and annular regimes (A). Here, the definitions of the flow regimes except for cap–slug flow are the same with those in a round pipe. In the cap–slug flow, the liquid phase is continuous, and the gas-phase flows in both small dispersed bubbles and cap/slug bubbles squeezed by the annulus walls. In Fig. 6, the flow conditions at $z/D_H = 52$, 149, and 230 are marked with symbols, and the corresponding flow regimes are given. These flow regimes are based on both the subjective visual observations and the area-averaged local flow parameters, such as local void fraction and IAC. The results in Fig. 6 show a good agreement with those of Juliá et al. (2007), which were obtained by using an objective neural network method. The method was developed by Mi et al. (2001), which used three impedance meters, one in each port, simultaneously. The sampling rate was 1000 Hz and the acquisition time was 60 s. The sets of the cumulative probability distribution function of the impedance probe signals for each flow condition and port were used for feeding a Kohonen self-supervised neural network.

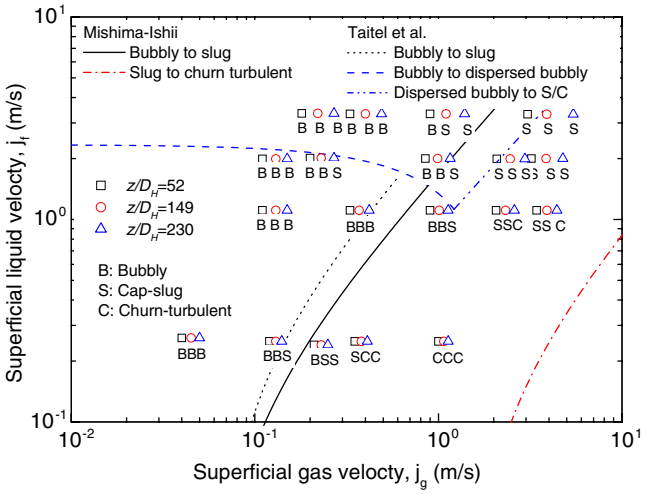

Fig. 6. The flow regimes at $z/D_H = 52$, 149 and 230: the local flow conditions are marked with symbols and the corresponding flow regimes are marked with B, S, or C.

It can be seen in Fig. 6 that there are some entrance effects in the flow-regime. For example, the flow at $z/D_H = 230$ of Run 2 ($\langle j_f \rangle = 0.25$ m/s and $\langle j_g \rangle = 0.14$ m/s) was a slug flow whereas the flow at $z/D_H = 52$ of Run 3 ($\langle j_f \rangle = 0.24$ m/s and $\langle j_g \rangle = 0.21$ m/s) was a bubbly flow. Similarly, the flow at $z/D_H = 230$ of Run 9 ($\langle j_f \rangle = 1.11$ m/s and $\langle j_g \rangle = 2.59$ m/s) was a churn–turbulent flow, but the flow at $z/D_H = 52$ of Run 10 ($\langle j_f \rangle = 1.11$ m/s and $\langle j_g \rangle = 3.43$) was a slug flow. This implies that a certain flow length is needed for bubble growth and flow-regime evolution, which clearly shows the limitation of static flow-regime maps and the necessity of the IAT approach, especially for developing flows. However, the bubbly-to-slug transition lines of Mishima and Ishii (1984) and Taitel et al. (1980), which were suggested for a flow in a round pipe, predict the transition in the annulus reasonably well.

3.3. Local flow structure

The local flow structure is mainly determined by bubble coalescence and breakup. The mechanism of bubble interactions can be summarized in five categories (Ishii and Hibiki, 2006): the coalescence due to random collisions driven by liquid turbulence; the coalescence due to wake entrainment, the breakup due to the impact of turbulent eddies, the shearing-off of small bubbles from cap/slug bubbles; and the breakup of large cap bubbles due to surface instability. Relative importance of these terms depends on flow conditions.

The radial migration of bubbles also plays an important role in the evolution of local flow structure. Zun (1988) studied transition from wall void peaking to core void peaking in turbulent bubbly flow in terms of bubble size, and suggested critical bubble sizes between the wall – intermediate – core void peaks. Tomiyama et al. (2002), Prasser et al. (2002), Lucas et al. (2005), and Krepper et al. (2005) also showed that small bubbles tend to move toward the wall, whereas large bubbles greater than 5.1–5.5 mm toward the center of the channel because the direction of the lift force is dependent on the bubble size. This results in the radial separation of small and large bubbles. This again affects the bubble interactions because they are radially not uniform but more active near the wall due to the higher turbulent intensity.

Figs. 7 and 8 show the radial distributions of time-averaged local void fraction and IAC at $z/D_H = 149$ for the nineteen conditions, respectively. In the sub-figures of Figs. 7 and 8, $\langle j_g \rangle$ increases from left to right, and $\langle j_f \rangle$ increases from bottom to top. These figures show global effects of $\langle j_g \rangle$ and $\langle j_f \rangle$ on local flow structures. By increasing $\langle j_g \rangle$, void fraction increases, i.e., the bubble density increases. This results in an increase in the bubble coalescence rate. If some bubbles become sufficiently large, they move toward the center of the annulus gap. Because of the low turbulent kinetic energy at the center, they have a less probability of breakup and can grow further by coalescence due to random collisions and wake entrainment. This mechanism is the key for the transition from bubbly-to-slug flow (Krepper et al., 2005). Meanwhile, by increasing $\langle j_f \rangle$, the dissipation rate of turbulent energy increases and, as a result, the frequency of bubble breakup increases. This generates small bubbles and, thus, the wall or intermediate peaking of void fraction.

For the tests under bubbly flows, the void fraction profiles of Run 1 and 2 have a center peak and the others have an intermediate peak. As mentioned earlier, the bubble diameter has a strong influence on the void fraction profile, and it is affected by the liquid velocity, which will be discussed later. Thus, for fully developed flows, the void fraction profile can be given in a map of $\langle j_f \rangle - \langle j_g \rangle$ plane. Serizawa and Kataoka (1988) suggested a simple model for phase distribution patterns in a vertical round pipe. Since their model was developed from fully developed flows, the evolution of bubble size was not taken into account. Lucas et al. (2005) also showed z/D_H-dependent phase distribution pattern maps, which were developed from the bubbly/slug flow data in a vertical pipe with an inner diameter of 51.2 mm and a length of 3 m. The trend of void fraction profiles in Fig. 7 is consistent with that of by Lucas et al. (2005) at $z/D_H = 59$.

The IAC, a_i, for a bubbly flow can be given by

$$a_i = 6\frac{\alpha_g}{D_S} \tag{2}$$

where α_g is the void fraction and D_S is the Sauter mean diameter. Therefore, the radial profiles of void fraction and IAC are very similar if D_S is radially uniform. However, the radial profile of D_S of Group 1 bubble always has a broad center peak (e.g., see Fig. 12). This yields a greater peak-to-average ratio in the measured IAC profile as can be seen in Fig. 8, if the void fraction profile is wall or intermediate peaked.

As shown in Figs. 7 and 8, the slug flows are characterized by high void fraction and low IAC, where the void fraction is center-peaked and the IAC is wall-peaked. This trend is getting more clear in the churn–turbulent flow regimes.

Table 2 shows the effect of $\langle j_g \rangle$ on the bubble count rate and the flow-regime at a constant $\langle j_f \rangle$ of 1.11 m/s. The bubble count rate means the area-averaged number of bubbles that were counted by the conductivity probe at the nine radial locations during one second. At low $\langle j_g \rangle$ conditions, the Group 1 bubble number increases along the channel due to the bubble breakup. However, when $\langle j_g \rangle$ reaches 0.90 m/s, coalescence occurs between $z/D_H = 149$ and 230. This results in a decrease of Group 1 bubbles and an increase of Group 2 bubbles, that is, a transition occurs from bubbly-to-slug flow. It can be seen that a significant number of Group 1 bubbles are agglomerated into Group 2 bubbles at slug flows of Run 9 and 10. If $\langle j_g \rangle$ is increased further, a flow transition occurs from slug to churn–turbulent flow. The transitions were not discrete but smooth until a certain flow condition.

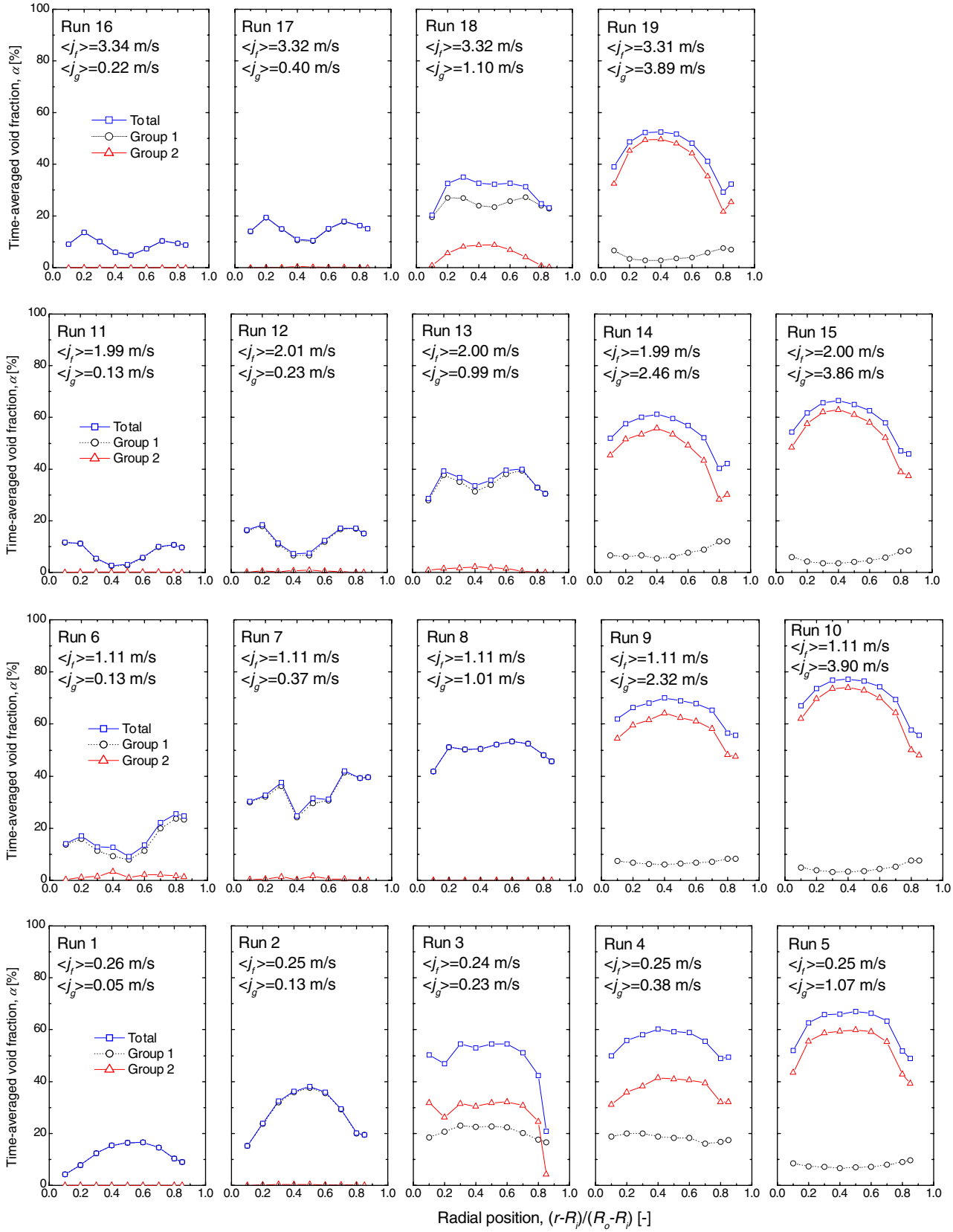

Fig. 7. Radial distributions of time-averaged void fraction at $z/D_H = 149$.

The effect of increasing $\langle j_f \rangle$ is clearly shown in the results of Run 16 ($\langle j_f \rangle = 3.34$ m/s and $\langle j_g \rangle = 0.18$ m/s at $z/D_H =$ 52). In Run 16, the flow regimes in the whole test section remained at bubbly flow and the average D_S of Group 1

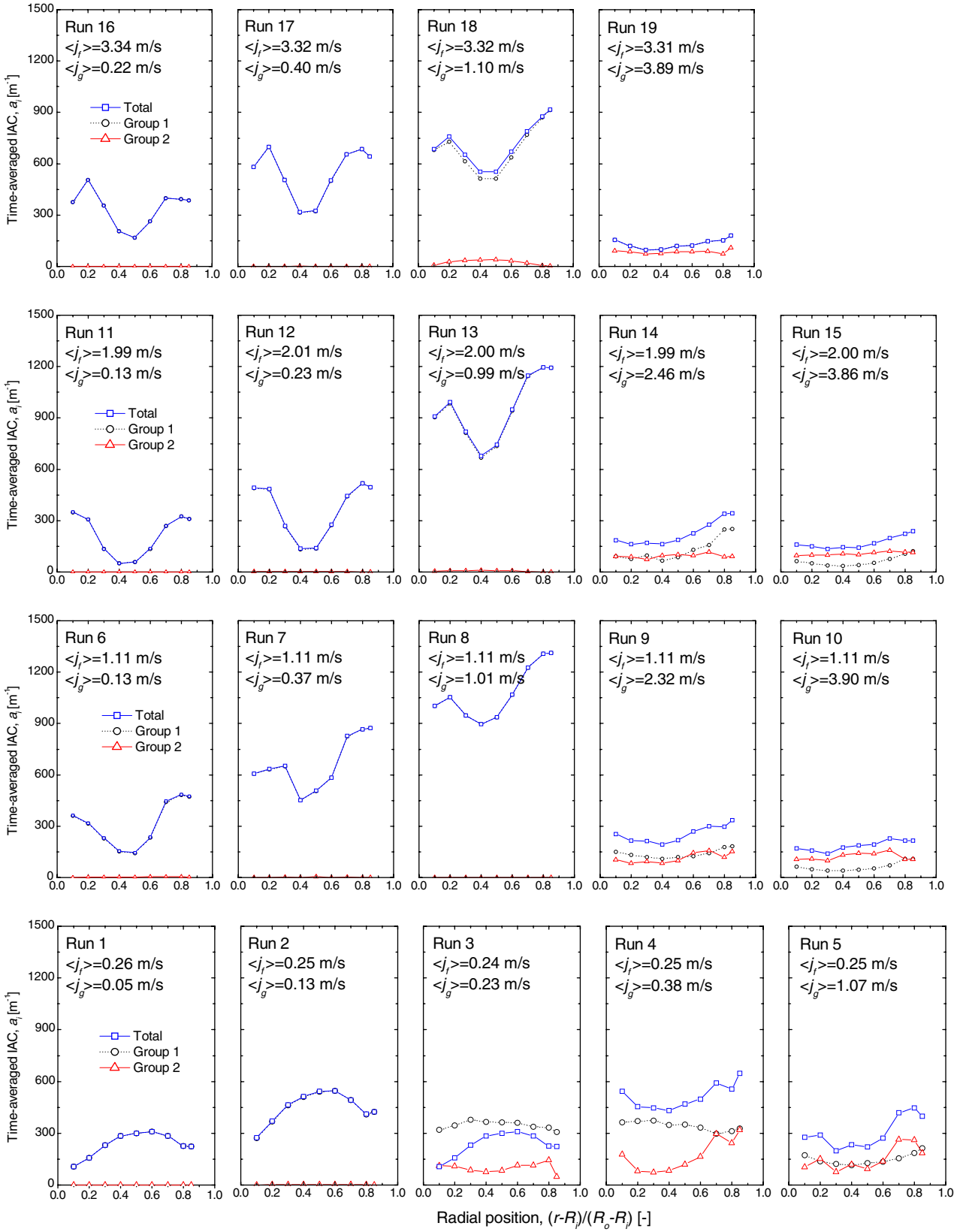

Fig. 8. Radial distributions of time-averaged IAC at $z/D_H = 149$.

bubbles were 1.6 mm. The radial void profiles of Run 16 at the three measurement ports are shown in Fig. 9a. They are intermediate peaked and the average void fraction slightly increases along the flow channel due to the expansion.

Table 2
Bubble count rate: effect of $\langle j_g \rangle$ with a constant $\langle j_f \rangle$ of 1.11 m/s

Run no.	$\langle j_g \rangle$ at $z/D_H = 52$	Group	Bubble count rate (s^{-1})			Flow regimes at $z/D_H = 52$, 149, and 230
			$z/D_H = 52$	$z/D_H = 149$	$z/D_H = 230$	
6	0.11	1	60.18	79.30	83.99	Bubbly/bubbly/bubbly
		2	0.27	0.80	0.71	
7	0.33	1	128.38	145.70	141.66	Bubbly/bubbly/bubbly
		2	0.04	0.26	0.03	
8	0.90	1	401.05	485.83	356.25	Bubly/bubbly/cap–slug
		2	0.00	0.01	6.33	
9	2.06	1	475.04	251.06	273.13	Cap–slug/cap–slug/churn–turbulent
		2	39.91	39.96	34.78	
10	3.43	1	217.52	130.89	116.34	Cap–slug/cap–slug/churn–turbulent
		2	45.62	43.54	44.84	

Since Group 2 bubbles do not exist in Run 16, all the bubble interactions attribute to breakup. Some bubble coalescences may occur, but the bubbles do not reach the size of a Group 2 bubble. Fig. 9b shows the radial profile of bubble count rates. It can be seen that the bubble breakup occurs actively near the outer wall. The area-averaged bubble count rates at $z/D_H = 52$, 149, and 230 are 106.7 s^{-1}, 122.2 s^{-1}, and 165.5 s^{-1}, respectively. This data is very useful for the fine tuning of the bubble breakup model for the source term of IAT equation.

Fig. 10 shows the probability distribution function (PDF) of the bubble chord length of Run 2, 6, 11, and 16 at $z/D_H = 149$. All these are at bubbly flow conditions. The PDF was retrieved from the conductivity probe signal. The bubble chord length decreases as a result of the bubble breakup when $\langle j_f \rangle$ is increased. The Sauter mean diameters at the conditions shown in Fig. 10 were 3.7 mm, 2.9 mm, 2.1 mm, and 1.6 mm from the bottom to the top, respectively. It is clear that D_S of Group 1 bubbles is inversely proportional to the liquid-phase velocity. As concerns the radial void fraction profile, Run 2 shows a center peak, whereas Runs 6, 11, and 16 show an intermediate peak. This is related with the bubble diameter. However, since the bubble diameter has a certain distribution at each flow condition, the critical bubble diameter that determines the radial profile cannot be clarified from this data. It is clear that, in Run 2, the fraction of the bubbles larger than 4.0 mm is significant.

Fig. 11 shows the PDF of the bubble chord length of Run 7, 8, 9, and 10 at $z/D_H = 230$, where $\langle j_g \rangle$ increases with a constant $\langle j_f \rangle$. In churn–turbulent flow-regime, i.e. the flow of Run 10 at $z/D_H = 230$, there were some bubbles, for which bubble chord lengths are between 0.2 m and 1.0 m. But these are not depicted in Fig. 11 because of very low frequency.

Fig. 12 shows the radial and axial distributions of local flow parameters of Run 13. The void profile of Group 1 bubbles becomes gradually flat along the channel. This is due to the higher coalescence rate near the walls. The Group 2 bubbles begin to be generated from $z/D_H = 149$ and its area-averaged void fraction reaches 12% at $z/D_H = 230$. The degree of the wall peaking of the Group 1 IAC is more distinct in comparison to that of the void profile, because of the smaller D_S of the Group 1 bubbles near the walls, as shown in Fig. 12c. For all the nineteen test conditions, the radial profiles of the D_S of the Group 1 bubbles are similar

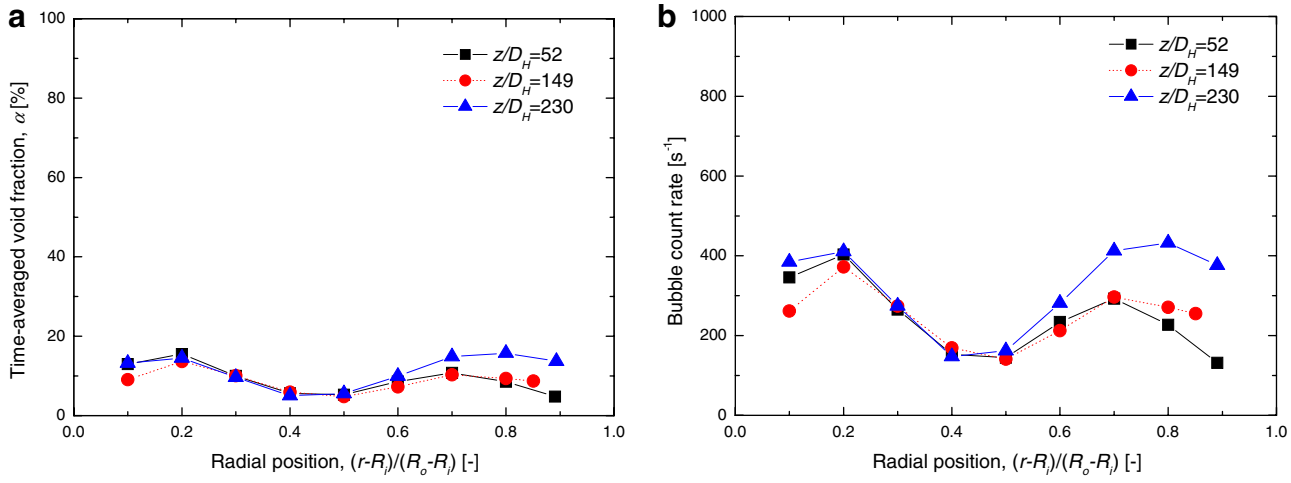

Fig. 9. The radial profiles of void fraction and bubble count rate of Run 16. (a) Void fraction (b) Bubble count rate.

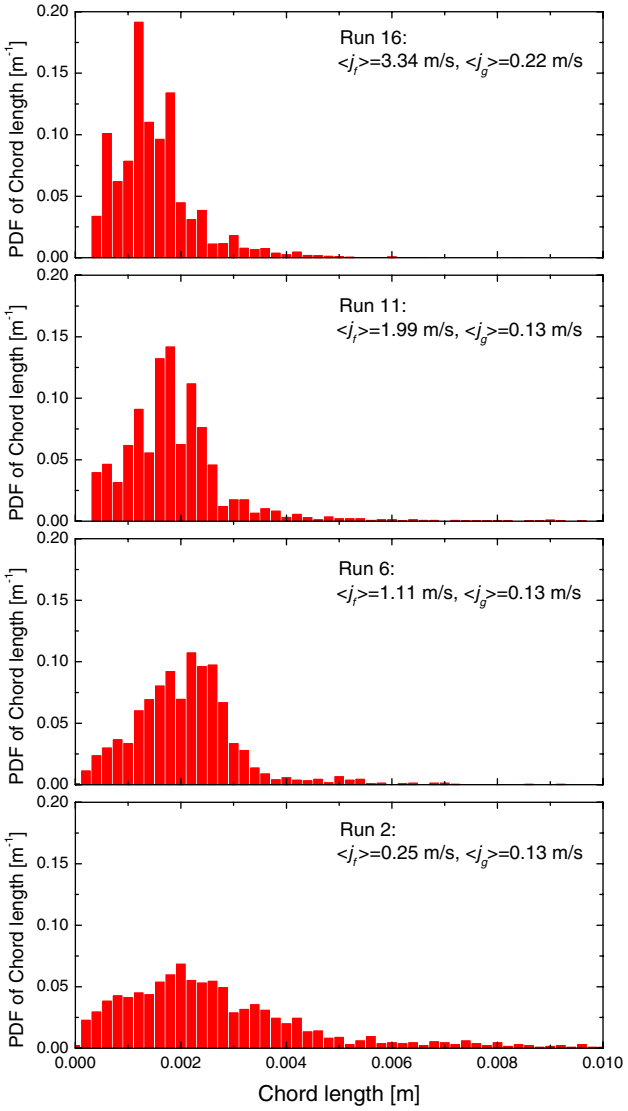

Fig. 10. The PDFs of the chord length of Run 2, 6, 11, and 16 at $(r - R_i)/(R_0 - R_i) = 0.7$ and $z/D_H = 149$.

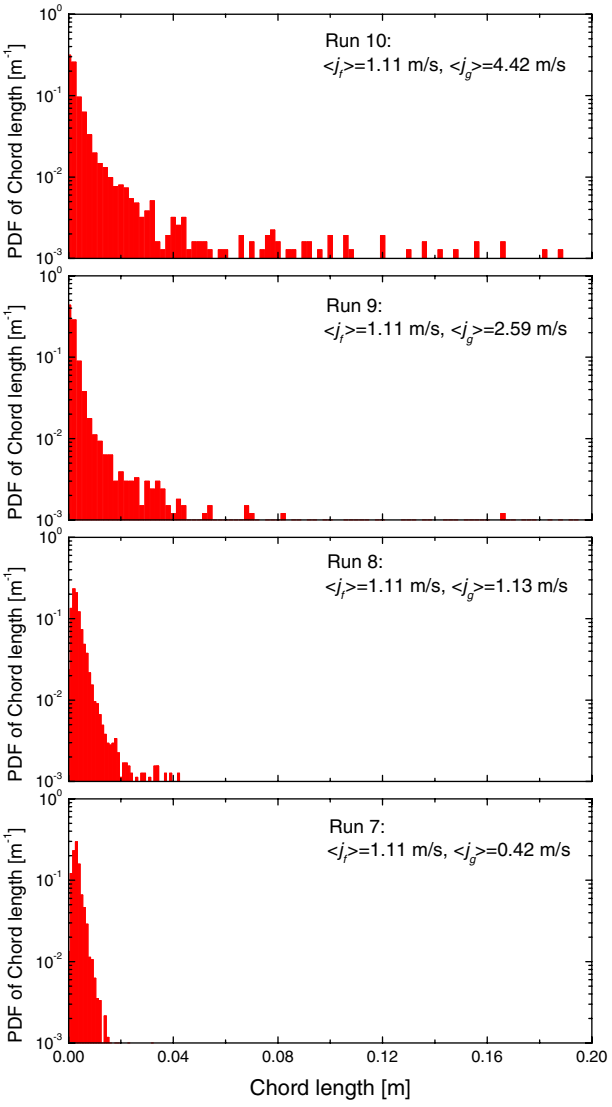

Fig. 11. The PDFs of the chord length of Run 7, 8, 9, and 10 at $(r - R_i)/(R_0 - R_i) = 0.7$ and $z/D_H = 230$.

to that in Fig. 12c, showing a broad center peak. This implies that the large bubbles tend to move toward the center. Fig. 12c also shows the average chord lengths of Group 2 bubbles, which become longer along the channel due to the bubble coalescence.

The interfacial velocity profiles at the three axial locations are shown in Fig. 12d and they are very similar to that of turbulent single-phase liquid flow (Quadrio and Luchini, 2002). Because of the finite size of the probe, the velocities near the walls could not be measured. Each velocity in Fig. 12d is the average of the interface velocities of all the bubbles that hit the conductivity probe. The standard deviation of the velocity fluctuation at $z/D_H = 230$ was 26.6%. The area-averaged velocity of Group 1 bubbles slightly increases along the channel.

It can be seen, from Figs 7–12 and Table 2, that the evolution of local flow structure is smooth to a certain extent and, for a given flow condition, the flow regime is determined by the degree of the progress toward an equilibrium point, which is balanced by bubble coalescence, breakup, and radial migration.

3.4. Axial evolution of the flow structure and interfacial area transport

Fig. 13 shows the axial profiles of the area-averaged void fraction. The steady-state one-dimensional continuity equation of the gas phase is given by

$$\frac{d}{dz}\left(\langle\alpha_g\rangle\rho_g\langle\langle v_g\rangle\rangle\right) = 0, \tag{3}$$

or

$$\frac{1}{\langle\alpha_g\rangle}\frac{d}{dz}\langle\alpha_g\rangle + \frac{1}{\rho_g}\frac{d}{dz}\rho_g + \frac{1}{\langle\langle v_g\rangle\rangle}\frac{d}{dz}\langle\langle v_g\rangle\rangle = 0, \tag{4}$$

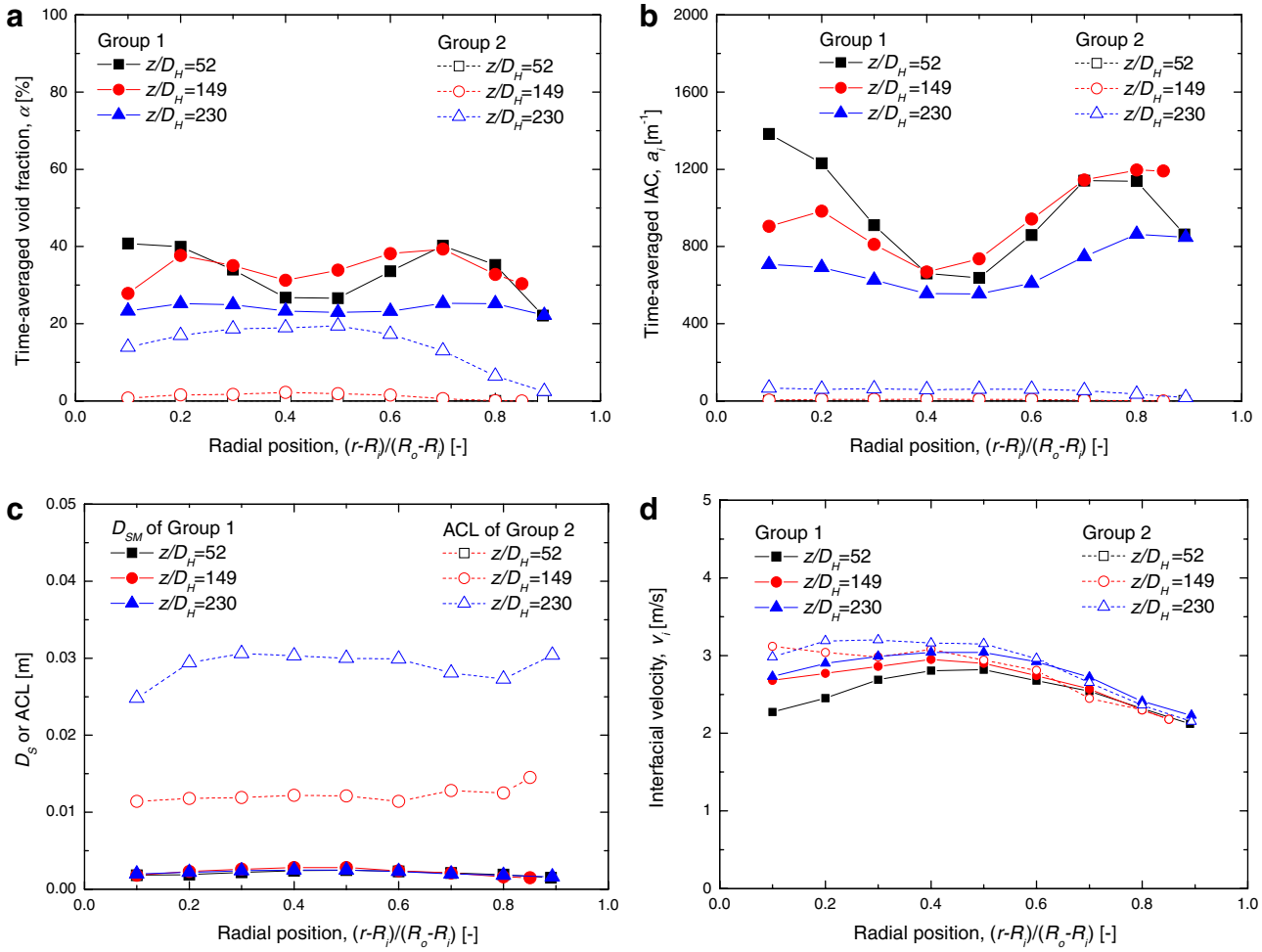

Fig. 12. The radial and axial distributions of local flow parameters of Run 13. (a) Void fraction (b) IAC (c) D_S or average chord length (ACL) (d) Interfacial velocity.

where $\langle\alpha_g\rangle$, ρ_g, and $\langle\langle v_g\rangle\rangle$ are area-averaged void fraction, density, and void-weighted area-averaged velocity, respectively. Using the ideal gas law for gas density, Eq. (4) is represented by

$$\frac{1}{\langle\alpha_g\rangle}\frac{d}{dz}\langle\alpha_g\rangle = -\frac{1}{P}\frac{d}{dz}P - \frac{1}{\langle\langle v_g\rangle\rangle}\frac{d}{dz}\langle\langle v_g\rangle\rangle \quad (5)$$

where P is pressure. The first term in the right-hand side (RHS) of Eq. (5) is always positive and it increases as the total mass flow rate increases. The second term in the RHS of Eq. (5) can be either positive or negative, but its effect decreases as the gas-phase velocity increases. As a whole, the area-averaged void fraction is expected to increase along the flow channel with the increase of total mass flow rate and/or gas-phase velocity. This trend can be seen in Fig. 13.

The axial profiles of area-averaged IAC are compared in Fig. 14. By considering the IAC data at $z/D_H = 52$ as boundary conditions, the data at $z/D_H = 149$ and 230 can be used for the development and assessment of IAT models. The cap–slug and churn–turbulent flows are characterized by a high void fraction and a low IAC. In general, because the contribution of Group 1 bubbles is dominant to total IAC, the total IAC is nearly proportional to the void fraction of Group 1 bubbles. This can be confirmed by comparing Figs. 13 and 14. However, the results of Run 18 with $\langle j_f\rangle = 3.32$ m/s are somewhat interesting. Fig. 13 shows the void fraction of Group 1 bubbles of Run 18 decreases and that of Group 2 increases along the flow channel, which means that there is bubble coalescence. However, in spite of the decrease of Group 1 bubble void fraction, the IAC of Group 1 bubbles increases because of the bubble breakup. This means both bubble coalescence and breakup occurred actively between $z/D_H = 149$ and 230.

4. Conclusions

An experimental study on the IAT of vertical, upward, air–water two-phase flows in an annulus channel has been performed. The inner and outer diameters of the annulus are 19.1 mm and 38.1 mm, respectively. Nineteen inlet flow

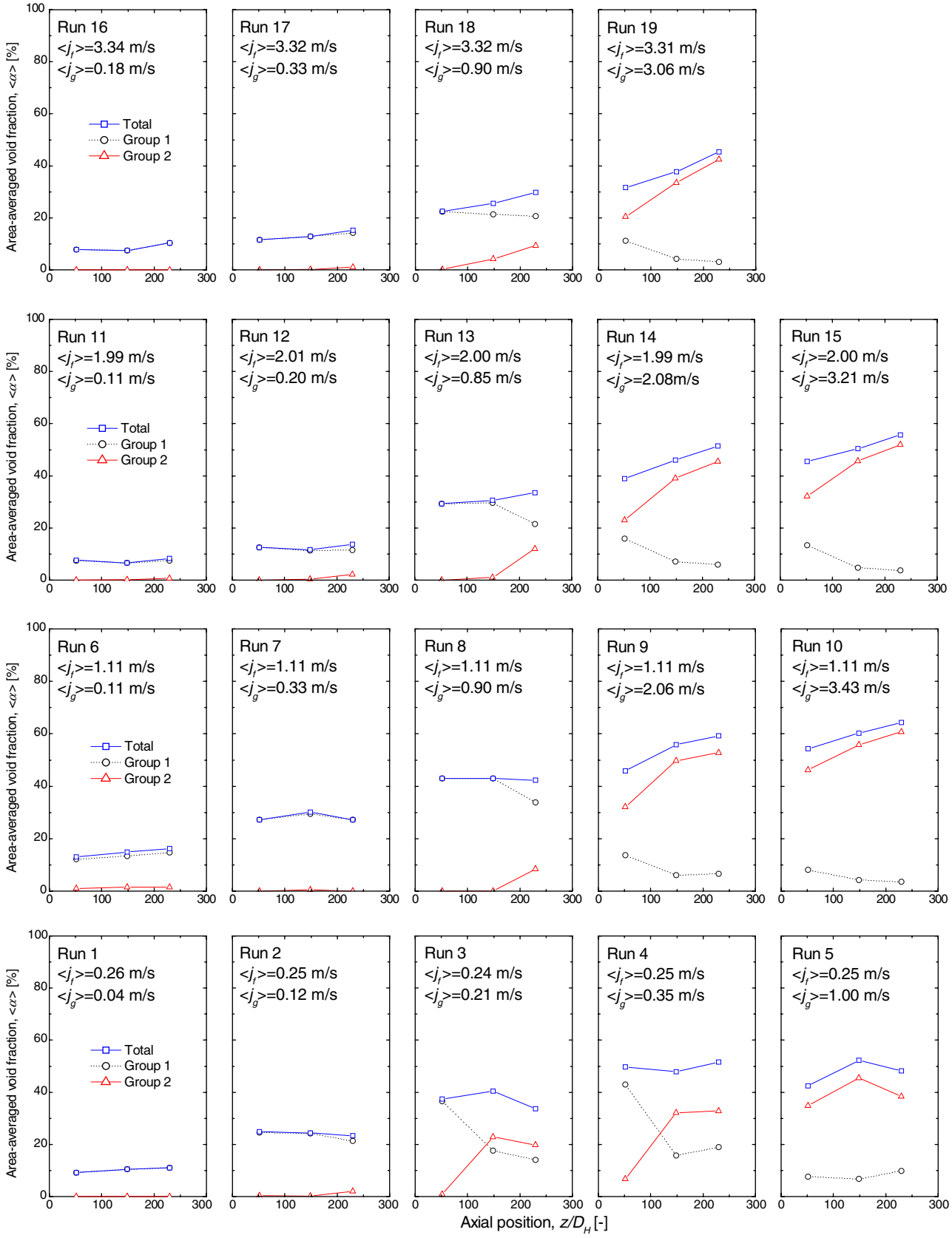

Fig. 13. Axial profiles of area-averaged void fraction: the flow conditions at $z/D_{\mathrm{H}} = 52$ are given.

conditions were selected so that a wide range of flow conditions could be covered, including bubbly, cap–slug, and churn–turbulent flows. Using the four-sensor conductivity probes, the local flow parameters were measured at nine

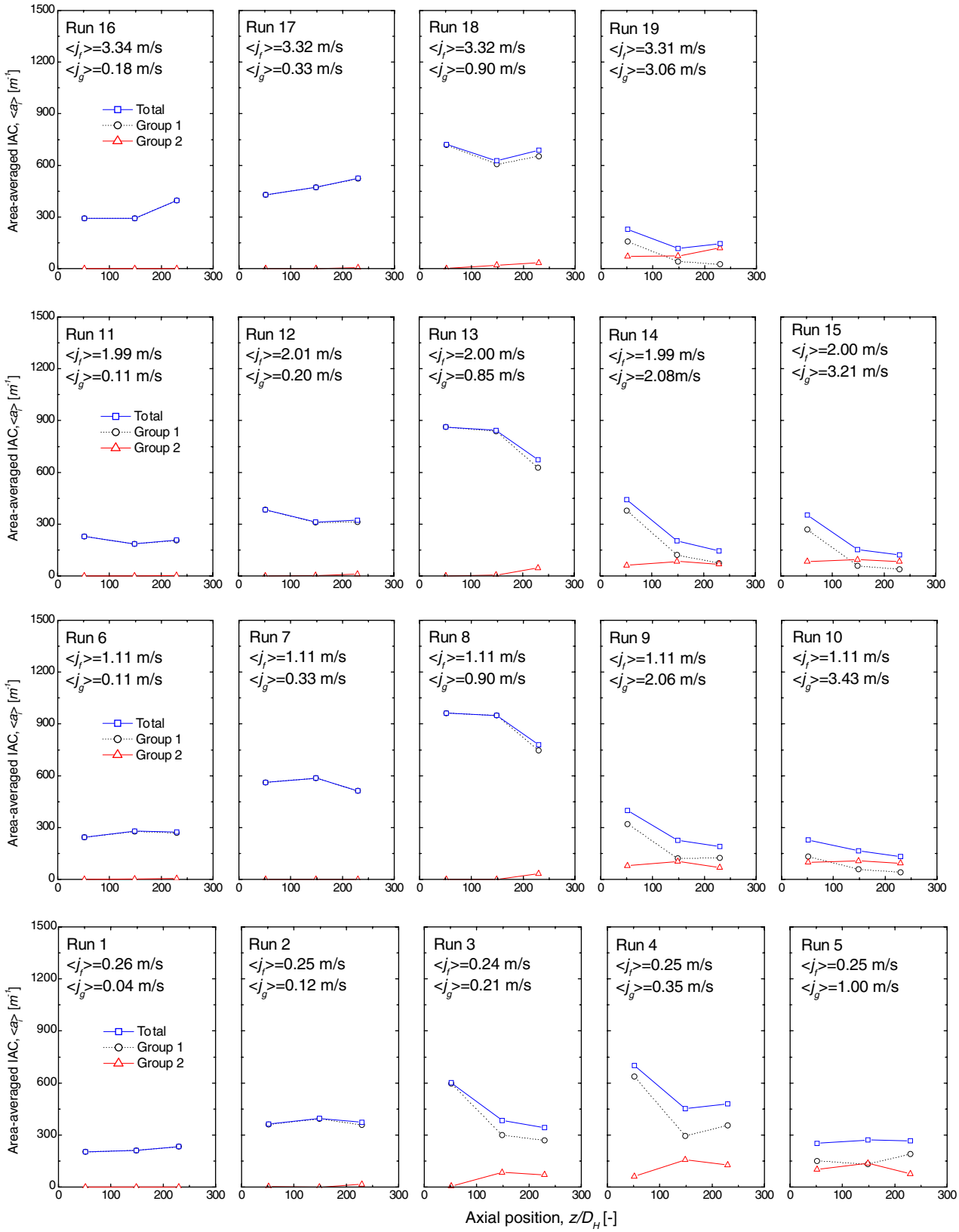

Fig. 14. Axial profiles of area-averaged IAC: the flow conditions at $z/D_H = 52$ are given.

radial positions for the three axial locations ($z/D_H = 52$, 149 and 230). The data include local void fractions, interfacial area concentrations, interfacial velocities, and bubble count rates for the two groups of bubbles.

Using the data for the nineteen conditions, the effects of $\langle j_g \rangle$, $\langle j_f \rangle$, and z/D_H on the local flow structure were analyzed. The data clearly showed the limitation of the static flow-regime maps and the necessity of the IAT approach, especially for developing flows. The effect of bubble diameter was also discussed and it was shown that small bubbles tend to move to the wall, and large bubbles to the center. Using the local bubble count rate, the radial and axial evolutions of IAC were interpreted in terms of bubble coalescence and breakup. Since the contribution of Group 1 bubbles to total IAC is dominant, the total IAC is nearly proportional to the void fraction of Group 1 bubbles. The slug and churn–turbulent flows were characterized by high void fraction and low IAC, where the void fraction is center-peaked and the IAC is wall-peaked. Even though this is obvious in the literature, very limited data supporting this fact quantitatively are available.

The measured data would be very useful for the development of the two-group IAT model, especially for the bubble coalescence and breakup models. Some of the data can be used for the fine tuning of individual source and sink terms of IAT equations. The data would be also suitable for the development of some closure models for computational fluid dynamics.

Acknowledgements

One of the coauthors, J.J. Jeong, would like to thank School of Nuclear Engineering, Purdue University. This work has been performed during his sabbatical leave at Purdue University under the financial support from Korea Atomic Energy Research Institute.

References

Bestion, D., 1990. The physical closure laws in the CATHARE code. Nucl. Eng. Design 124, 229–345.

Das, G., Das, P.K., Purohit, N.K., Mitra, A.K., 1999. Flow pattern transition during gas liquid upflow through vertical concentric annuli – Part I: experimental investigations. J. Fluids Eng. 121, 895–901.

Fu, X., 2001. Interfacial Area Measurement and Transport Modeling in Air–water Two-phase Flow, PhD Thesis, Purdue University, West Lafayette, Indiana, USA.

Grosstete, G., 1995. Experimental Investigation and preliminary numerical simulations of void profile development in a vertical cylindrical pipe. In: Second International Conference on Multiphase Flow, Tokyo, Japan, April 3–7, 1995.

Hibiki, T., Ishii, M., 1999. Experimental study on interfacial area transport in bubbly two-phase flows. Int. J. Heat Mass Transfer 42, 3019–3035.

Hibiki, T., Ishii, M., 2000. One-group interfacial area transport of bubbly flows in vertical round tubes. Int. J. Heat Mass Transfer 43, 2711–2726.

Hibiki, T., Hogsett, S., Ishii, M., 1998. Local measurement of interfacial area, interfacial velocity and liquid turbulence in two-phase flow. Nucl. Eng. Design 184, 287–304.

Hibiki, T., Takamasa, T., Ishii, M., 2001. Interfacial area transport of bubbly flow in a small diameter pipe. J. Nucl. Sci. Technol. 38, 614–620.

Hibiki, T., Mi, Y., Situ, R., Ishii, M., 2003. Interfacial area transport of vertical upward bubbly two-phase flow in an annulus. Int. J. Heat Mass Transfer 46, 4949–4962.

Ishii, M., 1975. Thermo-fluid Dynamic Theory of Two-phase Flow, Collection de la Direction den Etudes et Researches d'Electricite de France, Eyrolles, Paris, France, pp. 176–179.

Ishii, M., Hibiki, T., 2006. Thermo-fluid Dynamics of Two-phase Flow. Springer, New York, USA.

Ishii, M., Kim, S., 2001. Micro four-sensor probe measurement of interfacial area transport for bubbly flow in round pipes. Nucl. Eng. Design 205, 123–131.

Ishii, M., Kim, S., 2004. Development of one-group and two-group interfacial area transport equation. Nucl. Sci. Eng. 146 (3), 257–273.

Ishii, M., Zuber, N., 1979. Drag coefficient and relative velocity in bubbly, droplet or particulate flows. AIChE J. 25, 843–855.

Ishii, M., Kim, S., Kelly, J., 2005. Development of interfacial area transport equation. Nucl. Eng. Technol. 37, 525–536.

Juliá, J.E., Jeong, J.J., Dixit, A., Ozar, B., Hibiki, T., Ishii, M., 2007. Flow regime identification and analysis in adiabatic upward two-phase flow in an annulus geometry. In: 15th International Conference on Nuclear Engineering, Nagoya, Japan, April 22–26, 2007.

Kataoka, I., Ishii, M., Serizawa, A., 1986. Local formulation and measurement of interfacial area concentration in two-phase flow. Int. J. Multiphase Flow 12, 505–529.

Kelessidis, V.C., Dukler, A.E., 1989. Modelling flow pattern transitions for upward gas–liquid flow in vertical concentric and eccentric annuli. Int. J. Multiphase Flow 15, 173–191.

Kim, S., Fu, X., Wang, X., Ishii, M., 2000. Development of the miniaturized four-sensor conductivity probe and the signal processing scheme. Int. J. Heat Mass Transfer 43, 4101–4118.

Kim, S., Fu, X., Wang, X., Ishii, M., 2001. Study on interfacial structures in slug flows using a miniaturized four-sensor conductivity probe. Nucl. Eng. Design 204, 45–55.

Kocamustafaogullari, G., Ishii, M., 1995. Foundation of the interracial area transport equation and its closure relations. Int. J. Heat Mass Transfer 38 (3), 481–493.

Krepper, E., Lucas, D., Prasser, H.-M., 2005. On the modelling of bubbly flow in vertical pipes. Nucl. Eng. Design 235, 597–611.

Lucas, D., Krepper, E., Prasser, H.-M., 2005. Development of co-current air–water flow in a vertical pipe. Int. J. Multiphase Flow 31, 1304–1328.

Matijevic, E., 1969. Surface and Colloid Science. Wiley-Interscience, New York.

Mi, Y., Ishii, M., Tsoukalas, L.H., 2001. Flow regime identification methodology with neural networks and two-phase flow models. Nucl. Eng. Design 204, 87–100.

Mishima, K., Ishii, M., 1984. Flow regime transition criteria for upward two-phase flow in vertical tubes. Int. J. Heat Mass Transfer 27 (5), 723–737.

Morel, C., Goreaud, N., Delhaye, J.M., 1999. The local volumetric interfacial area transport equation: derivation and physical significance. Int. J. Multiphase Flow 25, 1099–1128.

Neal, L.G., Bankoff, S.G., 1963. A high resolution resistivity probe for determination of local void properties in gas–liquid flow. AIChE J. 9, 490–494.

Prasser, H.-M., Krepper, E., Lucas, D., 2002. Evolution of the two-phase flow in a vertical tube—decomposition of gas fraction profiles according to bubble size classes using wire-mesh sensors. Int. J. Therm. Sci. 41, 17–28.

Quadrio, M., Luchini, P., 2002. Direct numerical simulation of the turbulent flow in a pipe with annular cross section. Eur. J. Mech. B – Fluids 21, 413–427.

Revankar, S.T., Ishii, M., 1992. Local interfacial area measurement in bubbly flow. Int. J. Heat Mass Transfer 35, 913–925.

Revankar, S.T., Ishii, M., 1993. Theory and measurement of local interfacial area using a four sensor probe in two-phase flow. Int. J. Heat Mass Transfer 36, 2997–3007.

SCIENTECH, Inc., 1998. RELAP5/MOD3 Code Manual Volume I: code structure, system models and solution methods. Formerly NUREG/CR-5535. U.S. Nuclear Regulatory Commission.

Serizawa, A., Kataoka, I., 1988. Phase distribution in two-phase flow. In: Afgan, N.H. (Ed.), Transient Phenomena in Multi Phase Flow. Hemisphere, Washington DC, pp. 179–224.

Situ, R., Hibiki, T., Sun, X., Mi, Y., Ishii, M., 2004. Flow structure of subcooled boiling flow in an internally heated annulus. Int. J. Heat Mass Transfer 47, 5351–5364.

Smith, T.R., 2002, Two-group Interfacial Area Transport Equation in Large Diameter Pipes, PhD Thesis, Purdue University, USA.

Spore, J.W. et al., 1993. TRAC-PF1/MOD2 Code Manual, Volume I. Theory Manual, LA-12031-M, vol. I, NUREG/CR-5673, Los Alamos National Laboratory.

Sun, X., Kim, S., Ishii, M., Beus, S.G., 2004a. Modeling of bubble coalescence and disintegration in confined upward two-phase flow. Nucl. Eng. Design 230, 3–26.

Sun, X., Kuran, S., Ishii, M., 2004b. Cap bubbly-to-slug transition in a vertical annulus. Exp. Fluids 37, 458–464.

Taitel, Y., Borena, D., Dukler, E.A., 1980. Modelling flow pattern transitions for steady upward gas–liquid flow in vertical tubes. AIChE J. 26, 345–354.

Tomiyama, A., Tamai, H., Zun, I., Hosokawa, S., 2002. Transverse migration of single bubbles in simple shear flows. Chem. Eng. Sci. 57, 1849–1858.

Uhle, J., Wu, Q., Ishii, M., 1998. Dynamic flow regime modeling. In: Sixth International Conference on Nuclear Engineering (ICONE-6), May 10–14, 1998.

Wu, Q., Ishii, M., 1999. Sensitivity study on double-sensor conductivity probe for the measurement of interfacial area concentration for bubbly flow. Int. J. Multiphase Flow 25, 155–173.

Yao, W., Morel, C., 2004. Volumetric interfacial area prediction in upward bubbly two-phase flow. Int. J. Heat Mass Transfer 47, 307–328.

Zun, I., 1988. Transition from wall void peaking to core void peaking in turbulent bubbly flow. In: Afgan, N.H. (Ed.), Transient Phenomena in Multi Phase Flow. Hemisphere, Washington DC, pp. 225–245.